Nano Research

Open Access

Research Article

Constructing dual ion–electron transport channels via $Ti_3C_2T_x$ quantum-dot-embedded ZIF-8 for advanced Zn anodes

Man Li[1,§], Tao Chen[3,§], and Joonho Bae[1,2]✉

[1] Department of Physics and Semiconductor Science, Gachon University, Seongnam-si, Gyeonggi-do, 13120, Republic of Korea
[2] Department of Semiconductor Engineering, Gachon University, Seongnam, 13120, Republic of Korea
[3] School of Materials Engineering, Changzhou Vocational Institute of Industry Technology, Changzhou 213164, China
[§] Man Li and Tao Chen contributed equally to this work.

Cite this article: *Nano Research*, **2026**, *19*, 94908363. https://doi.org/10.26599/NR.2026.94908363

ABSTRACT: Uncontrolled dendrite growth and surface corrosion of Zn metal anodes severely hinder practical application of aqueous Zn-ion batteries (ZIBs). Herein, we propose a novel strategy to construct dual ion–electron transport channels by embedding $Ti_3C_2T_x$ quantum-dots (QDs) into a metal–organic framework (MOF) protective layer *in-situ* grown on the Zn surface. The zeolitic imidazolate framework-8 (ZIF-8) matrix provides well-defined sub-nanopores to guide Zn^{2+} flux uniformly while selectively blocking larger solvated Zn clusters, thereby suppressing dendrite growth, the hydrogen evolution reaction (HER), and corrosion. Meanwhile, highly conductive QDs, which act as electron mediators within the insulating ZIF-8, create interconnected electron pathways to accelerate charge transfer across the interface. As a result, the MOF@QD layer on the Zn anode enables stable Zn plating/stripping over extended cycles (1200 cycles at 1 mA·cm^{-2} and 2000 cycles at 5 mA·cm^{-2}) with reduced overpotential, dendrite-free morphology, and suppressed anode HER/corrosion. Zn//MnO_2 full batteries with MOF@QDs/Zn deliver an impressive high initial specific capacity of 277 mAh·g^{-1} at 0.2 A·g^{-1}, enhanced long-term capacity retention of 60% with ultra-high (99.5%) Coulombic efficiency (CE) after 500 cycles at 1 A·g^{-1}. This dual-channel design offers a generalizable approach for Zn-anode modification, paving the way for high-performance Zn-based energy storage systems.

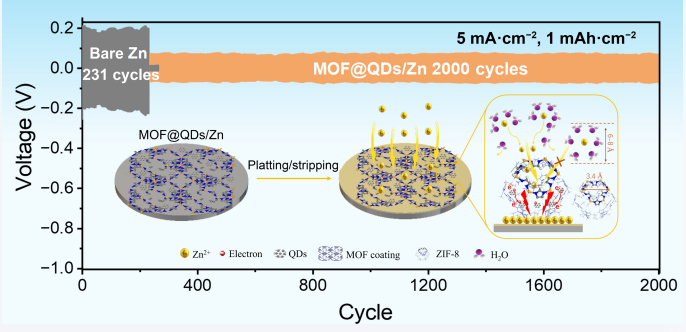

KEYWORDS: aqueous zinc-ion batteries, metal–organic framework, quantum-dot, electrode modification, dendrite suppression, solvation regulation

1 Introduction

Aqueous metal-ion batteries have shown potential for large-scale energy storage because of their safety, low cost, ease of processing, and high ionic conductivity [1–3]. Zinc metal exhibits a suitable redox potential (–0.76 V vs. standard hydrogen electrode (SHE)) along with highly reversible Zn/Zn^{2+} redox behavior in aqueous electrolytes, making it a suitable anode material for aqueous metal-ion batteries. More importantly, the Zn anode offers the intrinsic benefit of a high theoretical capacity, reaching 820 mAh·g^{-1} gravimetrically and 5854 mAh·cm^{-3} volumetrically [4–6]; therefore, the development of aqueous Zn-ion batteries (ZIBs) has attracted considerable research attention. However, uncontrollable dendrite growth on Zn anodes caused by non-uniform Zn^{2+} deposition during repeated plating/stripping remains a significant challenge, resulting in unstable Coulombic efficiency (CE), rapid capacity decay, and even short circuits of ZIBs [7, 8]. In addition, the hydrogen evolution reaction (HER), the dominant side reaction in ZIBs, can induce cell swelling by increasing internal pressure, which may pose significant safety risks in sealed battery systems [2]. As these issues hinder the practical application of ZIBs, various strategies have been developed to inhibit dendrite growth and side reactions, including the introduction of electrolyte additives [9, 10], structural design of electrodes [8, 11], and coating of protective layers on the Zn anode [12–14]. For instance, the work of Huang et al. has demonstrated that the trans fumaric acid (FU) as electrolyte additive with strong zincophilicity can modify solvation structure of Zn^{2+} and facilitate charge transfer to improve ZIB cycling stability

Received: October 10, 2025; **Revised:** December 5, 2025
Accepted: December 20, 2025

✉Address correspondence to baejh2k@gachon.ac.kr

[15]. In addition, various polymers, such as block polyether poloxamer [16], potassium hydrogen phthalate (KHP) [17], and imide derivatives (x-SU) [18], have been reported as electrolyte additives to enhance the performance of zinc anodes. Meanwhile, some strategies are studied for anode structural optimization. Inspired by natural surface architectures, a foldable three-dimensional (3D) MXene ($Ti_3C_2T_x$)/graphene aerogel composite (MXene–graphene aerogel (MGA)) was developed as a highly zincophilic 3D scaffold for Zn encapsulation [19]. ZnF_2-rich solid electrolyte interphase (SEI) formed at the anode/electrolyte interface induced by the terminal –F functional groups of MXene [20, 21], which effectively guides homogeneous Zn deposition, thereby suppressing the dendrite growth. Among these, applying a protective coating on the Zn anode represents a straightforward yet effective strategy to regulate the local electric field at the Zn surface and block direct interaction with H_2O molecules, thereby suppressing dendrite formation and mitigating side reactions [22]. For example, in the work of Liu et al., an MXene-cellulose nanofibrils (CNF) (MXene-CNF) composite hydrogel coated anode can contain the Zn volume changes, effectively homogenize Zn^{2+} flow and achieve a more uniform electric field distribution on the Zn anode surface [23]. Nevertheless, the reported artificial anode protection coatings on Zn anodes generally lack well-ordered and continuous Zn^{2+} transport pathways, which hinders efficient ion migration [13, 24, 25].

Metal–organic frameworks (MOFs) materials, with tunable porous structure, well-established 3D channels, and excellent mechanical strength [26–29], have been widely reported as the potential coating layer for the electrode and separator modification to effectively inhibit dendrite growth [30–33]. The tunable 3D porous structure within MOFs can provide ion transport pathways to facilitate Zn^{2+} ion migration while restricting the migration of big-sized solvated molecules, inducing uniform zinc deposition and suppressing HER. However, owing to the occasionality of manual coating, uncontrollable thickness and local inhomogeneities are difficult to avoid when using *ex-situ* coating, resulting in cracking or delamination during repeated Zn plating/stripping cycles or under high deposition loads. Most importantly, due to the extremely low bulk conductivity, MOFs commonly behave like an electrical insulator [34], resulting in sluggish electron movement and high polarizability, which greatly affects the electrochemical performance of zinc anodes at high current densities. Therefore, it is an effective solution to construct a protective layer with a uniform surface, high interfacial stability, and continuous pathways for both ion–electron transport.

In this work, $Ti_3C_2T_x$ quantum-dot (QD) assists zeolitic imidazolate framework-8 (ZIF-8) MOF to be *in-situ* synthesized on the surface of zinc foil, as shown in Fig. 1(a). Due to the polished Zn surface lacking defects and functional groups, it is difficult to nucleate the crystalline phase of ZIF-8 directly on a metal foil, which has to overcome a certain energy barrier. The charge negatived $Ti_3C_2T_x$ QDs possessing a high zincophilic property were introduced to form an adhesion layer, then work as a nucleation promoter and conductive bridge on the zinc foil, making it ideal for assisting the *in-situ* growth of ZIF-8 crystals on Zn surfaces. Benefiting from a self-limiting growth mechanism, the *in-situ* growing layer exhibits improved uniformity and interfacial stability [35]. Most importantly, the high-conductivity QDs embedded inside the ZIF-8 layer can act as the nanoelectronic highways to boost electron transport and effectively regulate the surface electric field, thus achieving uniform Zn deposition. To the best of our knowledge, this is the first construction of dual ion–electron transport channels on the Zn anode using an *in-situ* quantum-dot-embedded MOF coating method. This integrated design concept establishes the originality of this work and differentiates it from prior MOF-based protection strategies. The schematic deposition in Fig. 1(b) shows that, during the charging process of aqueous ZIBs with a bare Zn anode, a desolvation reaction of solvated zinc ions ($[Zn(H_2O)_6]^{2+}$) occurs, stripping off H_2O molecules [36, 37]. Reduced H_2O molecules with electrochemically reactive properties easily decompose when they accept electrons and release H_2 gas, which leads to potential safety hazards in sealed battery systems. As the HER occurs, a strongly alkaline environment is formed near the anode, leading to uncontrolled Zn corrosion [38, 39]. Therefore, we chose ZIF-8 MOF with a limited pore size of 3.4 Å as the layer matrix, which can restrict larger solvated clusters or solvent Zn

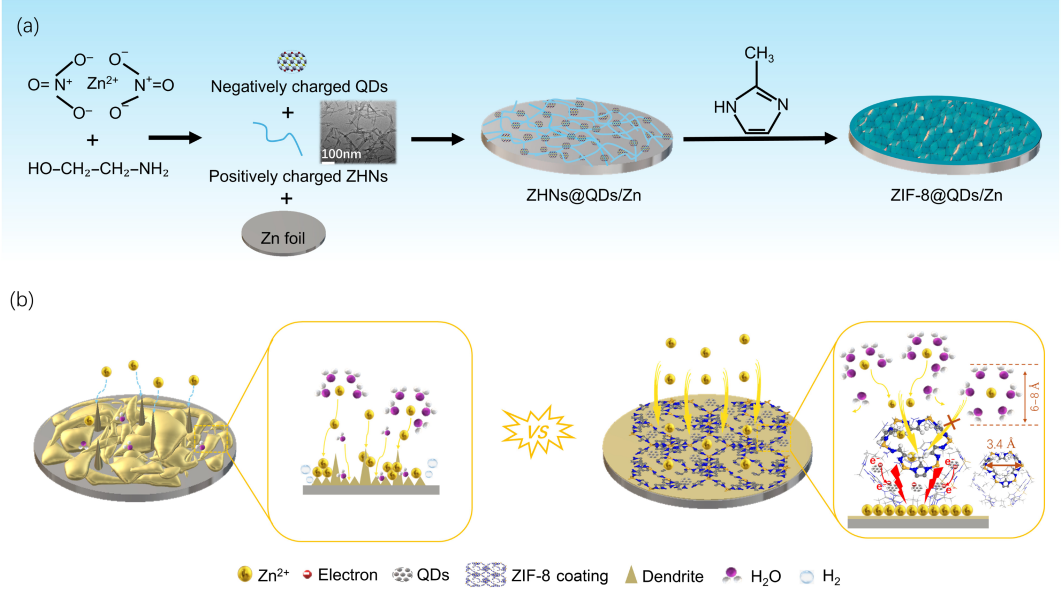

Figure 1 Schematic illustration of the Zn anode modification with MOF@QD microlayer. (a) The procedure of *in-situ*-grown MOF@QD layer on the Zn foil. (b) Schematic presentation of the Zn deposition behavior on bare Zn and MOF@QDs/Zn anode.

molecules (6–8 Å) from reaching the Zn surface [40], inhibiting side reactions of HER and Zn corrosion. Furthermore, the synthesized MOF@QD layer facilitates dual Zn ion–electron transport. ZIF-8 layers with well-defined pore apertures on the Zn anode can work as the ion channel for uniform Zn^{2+} flux, allowing fast Zn^{2+} diffusion. Meanwhile, QDs embedded inside the ZIF-8 layer provide continuous nanoelectronic highways to boost electron transport and enhance the electric field regulation on the Zn surface. Hence, the MOF@QD protective layer with a continuous 3D network enables uniform ion–electron flux during zinc deposition, thereby efficiently suppressing dendrite growth. As a result, a stable Zn plating/stripping over extended cycles of 1200 cycles at 1 mA·cm^{-2} and 2000 cycles at 5 mA·cm^{-2} was realized for MOF@QD modified Zn (MOF@QD/Zn) with dendrite-free morphology and suppressed anode HER/corrosion. Zn//MnO_2 full batteries with MOF@QDs/Zn deliver an impressive high initial specific capacity of 277 mAh·g^{-1} at 0.2 A·g^{-1}, enhanced long-term capacity retention of 60% with ultra-high (99.5%) CE after 500 cycles at 1 A·g^{-1}.

2 Experimental

2.1 Materials and chemicals

Zinc nitrate ($Zn(NO_3)_2·6H_2O$), 2-aminoethanol (NH_2-CH_2CH_2OH), and 2-methylimidazole (Hmim) ($C_4H_6N_2$) were purchased from Sigma-Aldrich. The $Ti_3C_2T_x$ QDs were supported by Nanjing Mingshan New Materials Technology Co., Ltd. 99.9% purified Zn foil with a thickness of 0.1 mm and 99.9% purified Ti foil with a thickness of 0.025 mm purchased from the MTI Korea Co., Ltd. Zinc sulfate heptahydrate ($ZnSO_4·7H_2O$) and anhydrous manganese sulfate ($MnSO_4$) were obtained from Sigma-Aldrich. α-MnO_2 was synthesized by a typical hydrothermal method according to a previously reported method [12, 41]. All other solvents and reagents used in this study were procured from commercial suppliers and were used without additional purification.

2.2 QD-assisted *in-situ* growth of ZIF-8 on Zn foil

First, a water–ethanol mixture (3:2 v:v) was prepared. Then $Zn(NO_3)_2·6H_2O$ (4 mM, Solution A) and 2-aminoethanol (1.6 mM, Solution B) were dissolved in the water–ethanol mixture. After complete dissolution, equal volumes of Solutions A and B were quickly mixed and aged for 30 min to synthesize zinc hydroxide nanostrands (ZHNs). 1 mL of QD (1 mg·mL^{-1}) aqueous solution was added and stirred for 60 s, after which a polished Zn foil was immersed into the mixture to obtain ZHNs@QDs on the surface. After 30 min, 25 mM of Hmim in water–ethanol (4:1 v:v) solution of twice the volume of Solution A was added. After static reaction at room temperature for 24 h, ZIF-8@QDs/Zn was obtained. The product was washed with water–ethanol solution three times and dried at 80 °C for 12 h, then punched into a round shape for testing. For comparison, the ZIF-8/Zn product was synthesized using the same approach without QDs. The *ex-situ* coating ZIF-8@QDs/Zn was also prepared using the doctor blade of a 10 and 20 μm gap after mixing ZIF-8@QDs and polyvinylidene fluoride (PVDF) in N-methyl-2-pyrrolidone (NMP) solvent with a mass ratio of 9:1.

2.3 Characterization

The morphology and structural features of the MOF@QD composite particles were characterized by transmission electron microscopy (TEM, Tecnai). The surface morphology of the modified Zn anode and the Zn deposition behavior were further examined using scanning electron microscopy (SEM, SU8600) coupled with energy-dispersive spectroscopy (EDS). Zeta potential measurements were performed using a nanoparticle tracking analyzer (Particle Metrix, PMX 120). X-ray diffraction (XRD) patterns were obtained using a high-resolution diffractometer (Rigaku SmartLab, Japan). X-ray photoelectron spectroscopy (XPS) analyses were performed on a Thermo Scientific™ K-Alpha™+ instrument equipped with a monochromatic Al Kα source (1486.6 eV) operated at 100 W.

2.4 Electrochemical measurements

CR2032 coin-type cells were assembled employing 200 μL of 2 M $ZnSO_4$ electrolyte and a glass fiber separator for the electrochemical measurements. Electrochemical impedance spectroscopy (EIS) was carried out using a Zahner IM6ex analyzer, with a frequency sweep from 0.01 to 10^5 Hz and an alternating current (AC) perturbation amplitude of 5 mV. Cyclic voltammetry (CV) measurements were performed within the potential range of 1.0–1.8 V. Linear polarization measurements were also conducted using a three-electrode setup to evaluate the corrosion behavior of Zn metal anodes. The potentiostatic polarization was performed at a constant potential of 0.1 V. Chronoamperometry (CA) analysis was carried out in a Zn||Zn symmetric cell with a potential of −150 mV. Galvanostatic charge–discharge (GCD) tests were conducted using a battery testing system (LAND, CT2001A). Zn plating/stripping behavior in the Zn||Ti half-cells was evaluated by cycling up to 1.0 V (vs. Zn^{2+}/Zn). The MnO_2 cathodes were fabricated by casting a slurry composed of MnO_2 active material, Super P carbon, and PVDF binder in a weight ratio of 6:3:1 onto Ti foil, then punched into 14 mm discs after vacuum drying under a mass loading of ~ 1 mg·cm^{-2}. GCD measurements of the Zn||MnO_2 full cells were carried out within the voltage range of 1.0–1.8 V (vs. Zn^{2+}/Zn).

3 Results and discussion

The $Ti_3C_2T_x$ QDs were first observed using the TEM image in Fig. S1 in the Electronic Supplementary Material (ESM), which exhibits a uniform size distribution of 5–10 nm. A high-resolution TEM (HRTEM) image further confirms the crystalline nature of the QDs. Clear lattice fringes with spacings of ~ 0.26 nm correspond to the (0100) planes of MXene QDs. The QD-assisted ZIF-8 coating layer was fabricated through a solid confinement conversion method at room temperature, as illustrated in Fig. 1(a). The negatively charged $Ti_3C_2T_x$ QDs (Zeta potential: −33.5 mV, Fig. S2 in the ESM) can firmly anchor the positively charged ZHNs (ZHNs@QDs), then ZHNs@QDs were transferred into ZIF-8 MOF@QDs composite layer on the Zn anode when immersing the ZHNs@QDs–Zn foil in an organic ligand (Hmim) solution. QDs help to localize nucleation at many tiny spots to avoid random, patchy ZIF-8 deposition, realizing uniform and controlled *in-situ* synthesis. Therefore, a ZIF-8@QDs film with a dense and uniform surface morphology (Figs. 2(a) and 2(b)) and a micro-layer thickness of around 5 μm (Fig. 2(c)) was successfully formed on the Zn surface. The comparative digital pictures in Fig. S3 in the ESM show the Zn foil surface before and after the *in-situ* growth of the MOF@QDs protective layer. However, when ZIF-8 was synthesized directly on the Zn anode, a polished zinc surface with short functional groups

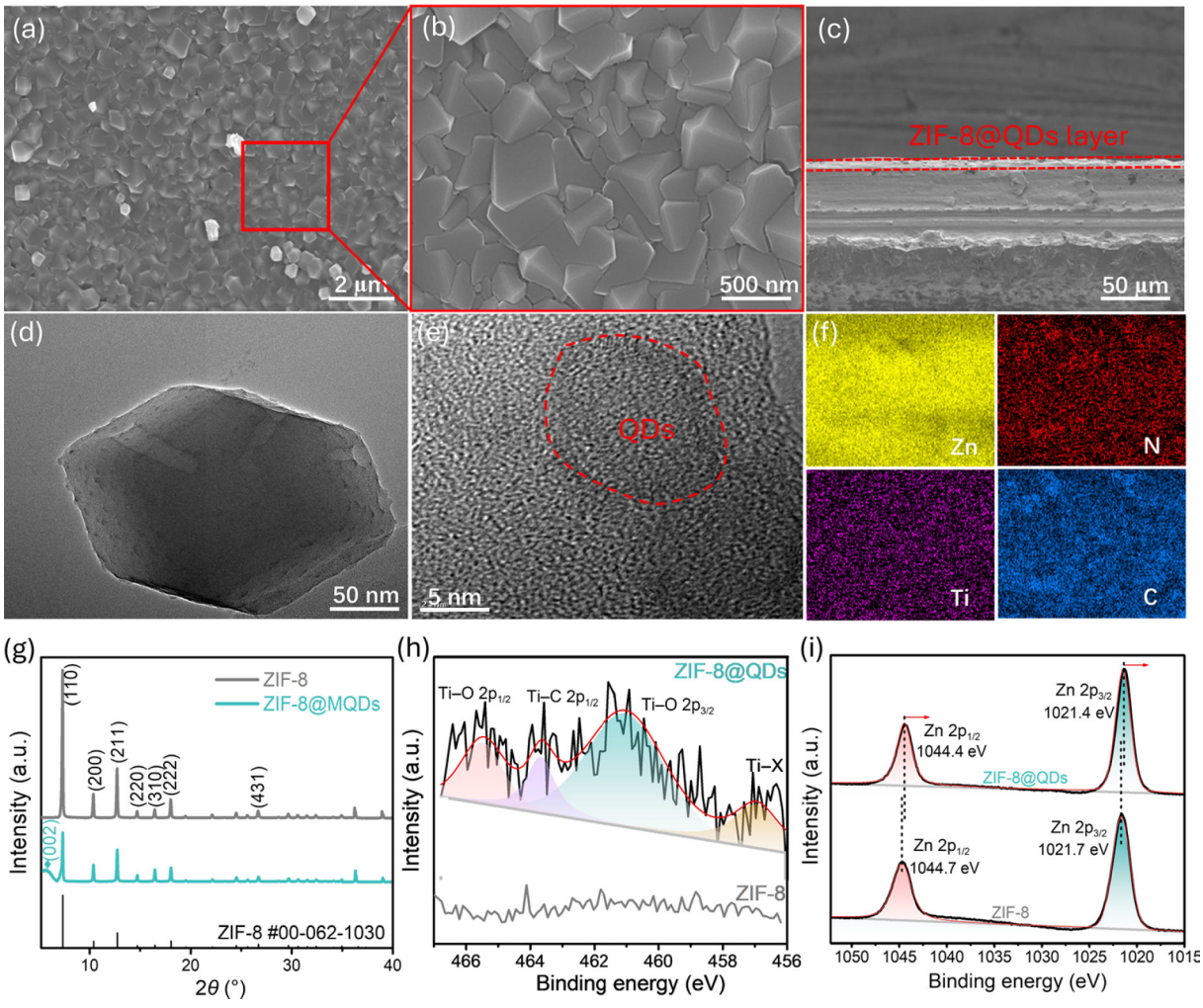

Figure 2 Characterization of the ZIF-8@QDs/Zn composite anode. ((a) and (b)) SEM images of the surface-view and (c) cross-section of ZIF-8@QD layer on the Zn anode. ((d) and (e)) TEM images showing the morphology characterization of ZIF-8@QDs (f) EDS mapping of ZIF-8@QDs/Zn with different elements. (g) XRD patterns and XPS spectra of (h) Ti 2p and (i) Zn 2p for ZIF-8 and ZIF-8@QDs composite.

and defective sites made homogeneous nucleation on the Zn foil difficult. As a result, a thick (~ 25 μm) but fairly loose MOF layer was stacked on the Zn substrate, as shown in Fig. S4 in the ESM. A thick insulating layer blocks electron transfer, and the loose structure carries the risk of shedding or delamination during Zn plating/stripping cycles. The TEM image in Fig. 2(d) shows well-defined hexagonal nanoparticles with a lateral size of ~ 200 nm and relatively smooth edges, indicating uniform crystal growth. The QD domain is highlighted by a red dashed circle in the HRTEM image (Fig. 2(e)), suggesting the successful incorporation of nanoscale features within the host matrix. The corresponding EDS elemental mapping in Fig. 2(f) confirms the homogeneous distribution of Zn, N, Ti, and C throughout the composite, further supporting the successful integration of $Ti_3C_2T_x$ QDs into the ZIF-8 framework. X-ray diffraction (XRD) and XPS were conducted to analyze the ZIF-8 MOF@QD composites in more detail. As shown by the XRD spectra in Fig. 2(g), diffraction peaks at approximately 7.3°, 10.4°, 12.7°, 14.7°, 16.5°, 18.0°, and 26.7° are observed for the pure ZIF-8 and ZIF-8 MOF@QDs samples, which correspond to the (110), (200), (211), (220), (310), (222), and (431) crystallographic planes of the ZIF-8 MOF, respectively. Apart from these typical peaks for MOF, another peak at 6° is observed for the MOF@QD composite and ascribed to the (002) planes of $Ti_3C_2T_x$ QDs, suggesting uniform and intimate coupling between the $Ti_3C_2T_x$ QDs and ZIF-8 MOF. The XPS profiles in Fig. S5 in the ESM show the main peaks of Zn 2p, O 1s, N 1s, and C 1s at 1023, 532, 396, and 284 eV, respectively. In the high-resolution Ti 2p XPS region, peaks located at 465.4, 461.7, 460.5, and 455.3 eV are observed (Fig. 2(h)) for the MOF@QD composite, representing Ti–O $2p_{1/2}$, Ti–C $2p_{1/2}$, Ti–O $2p_{3/2}$, and Ti–X (X = –F, –OH, and –O), respectively. No peak observed for the ZIF-8 in the same region. In addition, for the C 1s XPS spectrum of ZIF-8 @QDs (Fig. S6(a) in the ESM), peaks at approximately 284.5 and 286.3 eV are assigned to the C–C and C–O bonds, respectively. The peak at 288.5 eV (C=O) may be attributable to the oxidized functional groups of $Ti_3C_2T_x$ QDs or interfacial chemical reactions due to hybridization of ZIF-8 with $Ti_3C_2T_x$ QDs. The O 1s XPS spectrum (Fig. S6(b) in the ESM) could be deconvoluted into two species: C–Ti–O_x at 532.1 eV, and C–Ti–$(OH)_x$ at 531.0 eV. The N 1s spectrum (Fig. S6(c) in the ESM) features two characteristic peaks at 399.4 and 398.3 eV, ascribing to graphitic nitrogen and pyridinic nitrogen, which act as anchoring sites for Zn [42]. For the Zn XPS spectra in Fig. 2(i), two peaks at 1044.4 and 1021.4 eV were attributed to the Zn $2p_{1/2}$ and Zn $2p_{3/2}$ of Zn^{2+}, reflecting the existence of single Zn sites in ZIF-

8@QDs [43]. Besides, compared to the pure ZIF-8, a downshift of 0.3 eV appears at the Zn 2p peaks of MOF@QDs, implying an electron-rich environment due to charge transfer from $Ti_3C_2T_x$ QDs to ZIF-8 at the interface within the composite. In addition, the mass loading of $Ti_3C_2T_x$ QDs was semi-quantitatively determined from the XPS elemental composition (Table S1 in the ESM). The atomic percentage of 0.17 at.% corresponds to 0.40 wt.% of Ti mass loading. Therefore, the calculated $Ti_3C_2T_x$ QDs loading in the composite is around 1 wt.% in this work.

Chronoamperometry was first employed to systematically investigate the nucleation and growth behavior of Zn^{2+} deposition on different anode surfaces (Fig. S7 in the ESM). Under a constant potential, the time-dependent evolution of the deposition current sensitively reflects the nucleation kinetics and interfacial changes [44, 45]. For the bare Zn electrode, the current density continuously increases for approximately 400 s, indicating a prolonged two-dimensional (2D) diffusion-dominated stage. Such slow and uneven deposition ultimately leads to non-uniform growth and dendrite formation. In contrast, the MOF@QDs/Zn electrode completes nucleation and 2D diffusion within ~ 60 s and rapidly transitions into a stable 3D diffusion-controlled regime, demonstrating accelerated nucleation kinetics and more homogeneous Zn deposition. Notably, when MOF@QDs layers with thicknesses of 10 and 20 μm are applied onto Zn using an *ex-situ* coating process, the current continues to rise over time, suggesting a significantly prolonged 2D diffusion stage. This behavior indicates that the thicker coatings impose substantial Zn^{2+} transport resistance. Furthermore, the PVDF binder embedded within the artificial coating restricts ion-migration pathways and slows Zn^{2+} penetration toward the underlying metal surface, thereby delaying the transition from 2D nucleation/planar growth to 3D diffusion-controlled deposition. Zn anode stability was assessed by plating/stripping in Zn||Zn symmetrical cells at different current densities. The symmetrical battery with bare Zn showed unsatisfactory reversibility and experienced failure after only 205 (Fig. 3(a)) and 231 (Fig. 3(c)) cycles at current densities of 1 and 5 $mA·cm^{-2}$, respectively, due to internal short circuits caused by Zn dendrites (Figs. S8(a) and S8(b) in the ESM). An outstanding cycling stability of 1200 cycles at 1 $mA·cm^{-2}$ was demonstrated by symmetrical batteries with modified Zn in Fig. 3(a) and Fig. S8(c) in the ESM; however, a larger voltage hysteresis was observed for MOF/Zn at both 1 and 5 $mA·cm^{-2}$ due to sluggish Zn^{2+}/electron diffusion kinetics and high interfacial resistance of the anode caused by a thicker MOF layer. During the last plating period at 5 $mA·cm^{-2}$ (Fig. 3(c) and Fig. S8(d) in the ESM), the loose MOF layer may have collapsed and fallen into the electrolyte, resulting in a loss of the protection of the anode and polluting the electrolyte, leading to battery failure after 460 h (1140 cycles). Notably, the symmetrical cell with MOF@QDs/Zn demonstrated consistent and stable deposition processes across over 1200 h (1200 cycles) and 800 h (2000 cycles) at current densities of 1 and 5 $mA·cm^{-2}$, as illustrated in Figs. 3(a) and 3(c) and Figs. S8(e) and S8(f), respectively. This remarkable stability is attributed to the rapid ion/electron transfer and enhanced kinetics of zinc deposition and stripping induced by the dual-conduction system of the MOF@QD layer. In addition, the rate performance of the symmetrical cells based on the MOF@QDs/Zn composite anode exhibited excellent performance at a current density range of 0.25–5 $mA·cm^{-2}$ for 20 cycles (Fig. 3(e)). The cell with MOF@QDs/Zn exhibited a steadily increasing overpotential when the current density was increased from 0.25 to 5 $mA·cm^{-2}$. Meanwhile, the MOF@QDs/Zn continued to deliver stable stripping/plating with steadily decreasing voltage hysteresis when the current density returned to 0.25 from 5 $mA·cm^{-2}$, suggesting favorable reversibility and low polarization of the MOF@QDs/Zn anode. Excellent long-term stability of the MOF@QDs-Zn composite anode was achieved for 200 cycles at the high current density of 10 $mA·cm^{-2}$ (5 $mAh·cm^{-2}$), as shown in Fig. 3(g). The remarkable cycling improvement of the MOF@QDs/Zn anode is due to the construction of dual ion–electron transport channels, which ensure uniform Zn deposition, fast charge transfer, and suppressed parasitic reactions. A comparison of the symmetrical cell performance with that of various previously reported Zn metal composite anodes [11, 12, 14, 46–58] is shown in Fig. 3(h) and Table S2 in the ESM. Impressively, the cumulative plating capacity (CPC) of MOF@QDs/Zn in our work is enhanced, especially at high current density (10 $mA·cm^{-2}$), surpassing most reported results of ZIBs based on anode modification. In addition, compared with many reported coating methods that rely on multi-step synthesis or complex and high-cost coating procedures (Fig. S2 in the ESM), our $Ti_3C_2T_x$ QDs embedded ZIF-8 layer is prepared via a mild, solution-based *in-situ* growth on Zn anode, without the need for high-temperature annealing, vacuum equipment, or long-duration epitaxial processes, which offers a more straightforward and potentially scalable route to construct dual ion–electron transport channels.

The CE of the different anodes was determined from the plating/stripping voltage profiles of Zn||Cu half-cells operated at 2 $mA·cm^{-2}$ with a capacity of 1 $mAh·cm^{-2}$ (Fig. 3(b)). The bare Zn electrode exhibited rapid failure within 40 cycles, benefiting from the well-defined nanopores of the MOF layer that regulate Zn^{2+} ion flux. The MOF-modified Zn anode maintained stable plating/stripping performance for more than 200 cycles. However, the insulating nature of MOFs often limits electron transport, whereas embedded QDs provide conductive pathways within the coating. This ensures efficient stripping of the plated Zn without forming residual clusters trapped under the insulating layers, further improving the reversibility and CE. Therefore, the MOF@QDs/Zn delivered remarkable plating/stripping performance, achieving a high average CE of 99.7% over 400 cycles. In addition, from the initial CE of Zn||Cu cells, the cell with an MOF@QDs/Zn anode achieved an improved initial CE of 92.0% when compared to MOF/Zn (88.5%) and bare Zn (86.3%), as shown in Fig. 3(d). This is attributed to a lower nucleation barrier via zincophilic QDs, and a dual transport network lowers charge‾ transfer losses within the micro-layered MOF@QDs from the initial stage. Meanwhile, the minimal polarization fluctuations of only 101.4 mV for MOF@QDs/Zn observed from the plating/stripping voltage curves (Fig. 3(f)) could further substantiate this inference. Conversely, high voltage hysteresis of bare Zn (304.6 mV, Fig. S9(a) in the ESM) and MOF/Zn (171.1 mV, Fig. S9(b) in the ESM) is obtained owing to high polarization. Additional CE tests were performed using Zn||Cu cells under a high current density of 10 $mA·cm^{-2}$ (5 $mAh·cm^{-2}$) and lean-electrolyte conditions (100 μL). As shown in Fig. S10(a) in the ESM, the Zn||Cu cell with a bare Zn anode was short-circuited after only 3 cycles. For the MOF/Zn anode (Fig. S10(b) in the ESM), a high voltage polarization of 310 mV was observed, and short-circuiting occurred after 58 cycles, corresponding to a CE of 99.12%. In contrast, the ZIF-8@QDs/Zn anode maintained a high CE of 99.72% for 67 cycles, with a much lower voltage polarization of

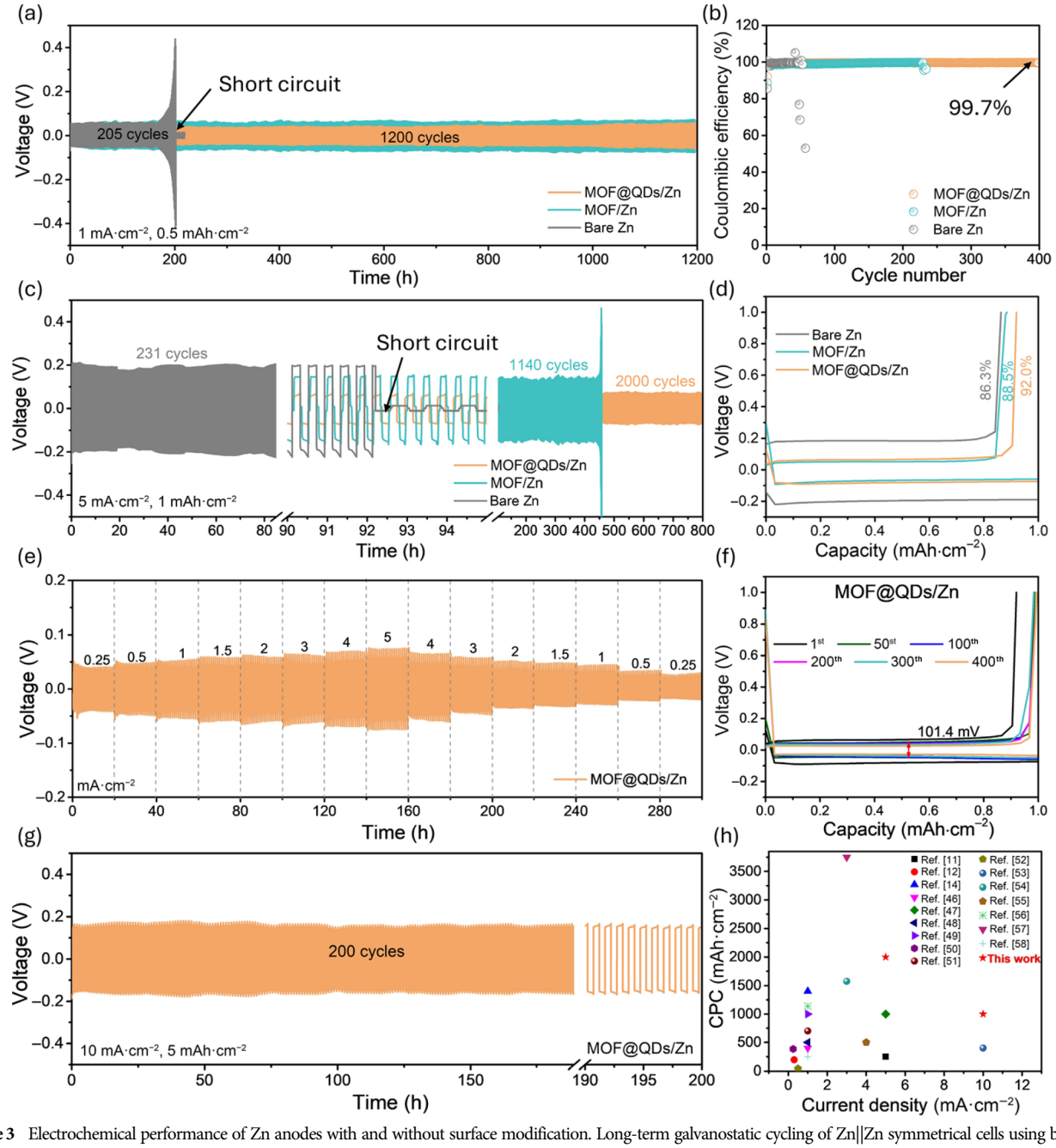

Figure 3 Electrochemical performance of Zn anodes with and without surface modification. Long-term galvanostatic cycling of Zn||Zn symmetrical cells using bare Zn, MOF/Zn, and MOF@QDs/Zn electrodes at current densities of (a) 1 mA·cm^{-2} and (c) 5 mA·cm^{-2}. (b) Coulombic efficiency of Zn||Cu half-cells. (d) Initial voltage profiles of Zn plating/stripping in Zn||Cu half-cells with bare Zn, MOF/Zn, and MOF@QDs/Zn at 2 mA·cm^{-2}. (e) Rate performance of symmetrical battery with MOF@QDs/Zn anodes. (f) Voltage profiles of Zn plating/stripping on Cu foil for MOF@QDs/Zn at different cycle numbers. (g) Long-term Zn plating/stripping of a symmetrical battery with MOF@QDs/Zn at a high current density of 10 mA·cm^{-2} (5 mAh·cm^{-2}). (h) Comparison of the cumulative plating capacity of the MOF@QDs/Zn symmetrical cell with previously reported anode modification strategies [11, 12, 14, 46–58].

130 mV, demonstrating its superior interfacial stability under more demanding cycling conditions (Figs. S10(c) and S10(d) in the ESM). Moreover, the MOF scaffold physically distances bulk H_2O from the metal while QDs help maintain electronic homogeneity, reducing both the HER and surface corrosion, as shown by a negatively shifted potential and reduced current in linear sweep voltammetry (LSV) curves (Fig. S11 in the ESM) associated with the HER, thereby contributing to a more stable Zn anode.

To further investigate the influence of the MOF@QD microlayer on Zn deposition, *in-situ* optical microscopy was employed to monitor the Zn deposition behavior and compare the dendrite growth on different anodes with and without modification (Figs. 4(a)–4(c)). Figure 4(a) shows that after only 5 min of Zn plating at a current density of 5 mA·cm^{-2}, small protrusions appear on the surface of bare Zn caused by inhomogeneous zinc deposition. As the time increases to 30 min, a rather rough and uneven Zn surface with obvious dendrites is observed, which dramatically shortens the lifetime of the Zn anode, leading to a short circuit of the battery. Compared to bare Zn, dendrite formation is significantly suppressed on the MOF/Zn surface

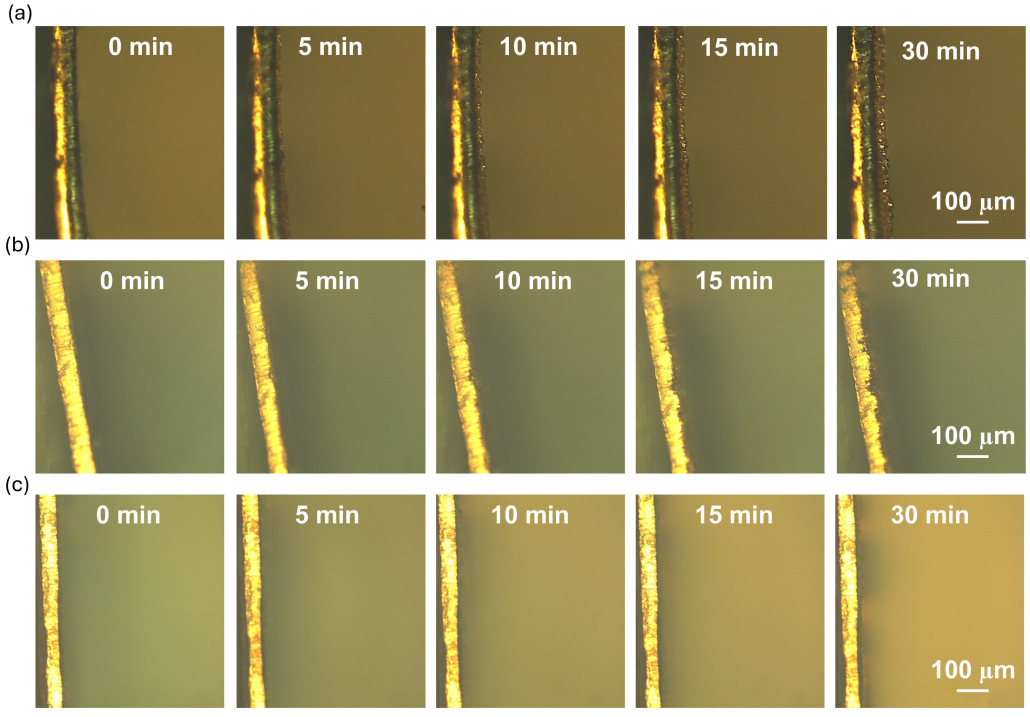

Figure 4 *In-situ* optical images of (a) bare Zn, (b) MOF/Zn, and (c) MOF@QDs/Zn anodes at 5 mA·cm^{-2}.

during Zn deposition because the ZIF-8 layer can serve as an ion-sieving barrier that hinders dendritic tip propagation. Meanwhile, the thick MOF layer on the Zn surface acts as a physical barrier that blocks the outward growth of sharp dendrites. However, a loose and thick MOF layer with poor electronic conductivity and poor interfacial contact conditions induces non-uniform current pathways and stagnant electrolyte regions. These factors accelerate localized corrosion and result in a rough, uneven Zn surface despite the absence of prominent dendrites, as shown in Fig. 4(b). In detail, in a thick, loosely packed layer, non-uniform electrons diffuse and reach the Zn surface through a few cracks or defects. These contact points become current hotspots, where local Zn stripping/plating intensifies, leading to deep pits and raised nodules. In addition, the loose ZIF-8 layer does not conform tightly to the Zn substrate, and cracks and collapse may occur during Zn deposition. Therefore, the electrolyte seeps underneath and reaches the Zn surface, where crevice corrosion zones are created to accelerate the HER and raise the local alkalinity, resulting in severe local Zn corrosion. In contrast, over the entire 30 min Zn plating process, the MOF@QDs/Zn surface maintains a smooth and compact morphology with no obvious dendrite growth (Fig. 4(c)). Uniform Zn deposition indicates simultaneous regulation of ion flux and electron conduction. The presence of $Ti_3C_2T_x$ QDs embedded within the MOF framework enhances interfacial charge transfer, reduces local current density fluctuations, and synergistically promotes homogeneous nucleation. At the same time, a tightly conformed MOF@QDs microlayer on the Zn substrate suppresses under‑film corrosion and the HER, hence no Zn corrosion is observed over 30 min.

High-resolution images of the Zn anodes' morphologies were characterized by SEM after 50 cycles of plating/stripping at 5 mA·cm^{-2}. In addition, the thicknesses of the symmetrical cells before and after cycling were measured to further quantify the HER. In the SEM images of bare Zn, a large area of the Zn surface contains vertical bumps and scrapes clustered together, suggesting that severe dendrite growth occurred at the anode (Fig. 5(a1)). Meanwhile, Zn metal corrosion extended along the surface to deeper layers below the surface, as shown in the cross-sectional image (Fig. 5(a2)). For the cycled MOF/Zn anode, a certain number of cracks are distributed on the surface (Figs. 5(b1) and 5(b2)), because the loose and thick MOF layer is fractured during plating/stripping, leading to electrolyte seepage along the cracks and reaching the Zn surface to accelerate the HER and local Zn corrosion. Therefore, the SEM results agree well with the *in-situ* optical observations shown in Fig. 4(b). In contrast, a smooth and continuous deposition layer is formed on the MOF@QDs/Zn anode (Figs. 5(c1) and 5(c2)), and almost no dendrite growth is observed on the surface of the cycled anode. The MOF@QDs coating retained excellent mechanical integrity after cycling. The cross-sectional SEM images reveal continuous coating without any cracks or delamination. This robustness is primarily attributed to the intrinsic mechanical advantages arising from the combination of the ZIF-8 framework (rigid tetrahedral topology) and the $Ti_3C_2T_x$ quantum-dots. Their synergistic interaction enhances interfacial cohesion and effectively mitigates the volume fluctuations of the Zn anode during the plating/stripping process. The changes in cell thickness were compared to evaluate the H_2 gas released from the HER side reactions in the batteries. As shown in Figs. 5(a3) and 5(b3), the thickness increases were 3.2% and 1.2% for the coin cells with bare Zn and MOF/Zn, respectively, indicating the occurrence of HER. The smallest thickness change of 0.9% was obtained for the cell with the MOF@QDs/Zn anode (Fig. 5(c3)), indicating that the HER was significantly suppressed. The suppression of Zn corrosion by the MOF and MOF@QD films was further evaluated using linear polarization tests in a 2 M $ZnSO_4$ solution (Fig. 5(d)). MOF@QDs/Zn exhibited a higher corrosion potential (−0.983 V) than those of MOF/Zn and bare Zn (−0.986 and −0.990 V, respectively), suggesting an enhanced anticorrosion ability [59]. XRD analysis was performed to determine the surface composition of the cycled Zn electrodes (Fig. 5(e)). The (002) peak from

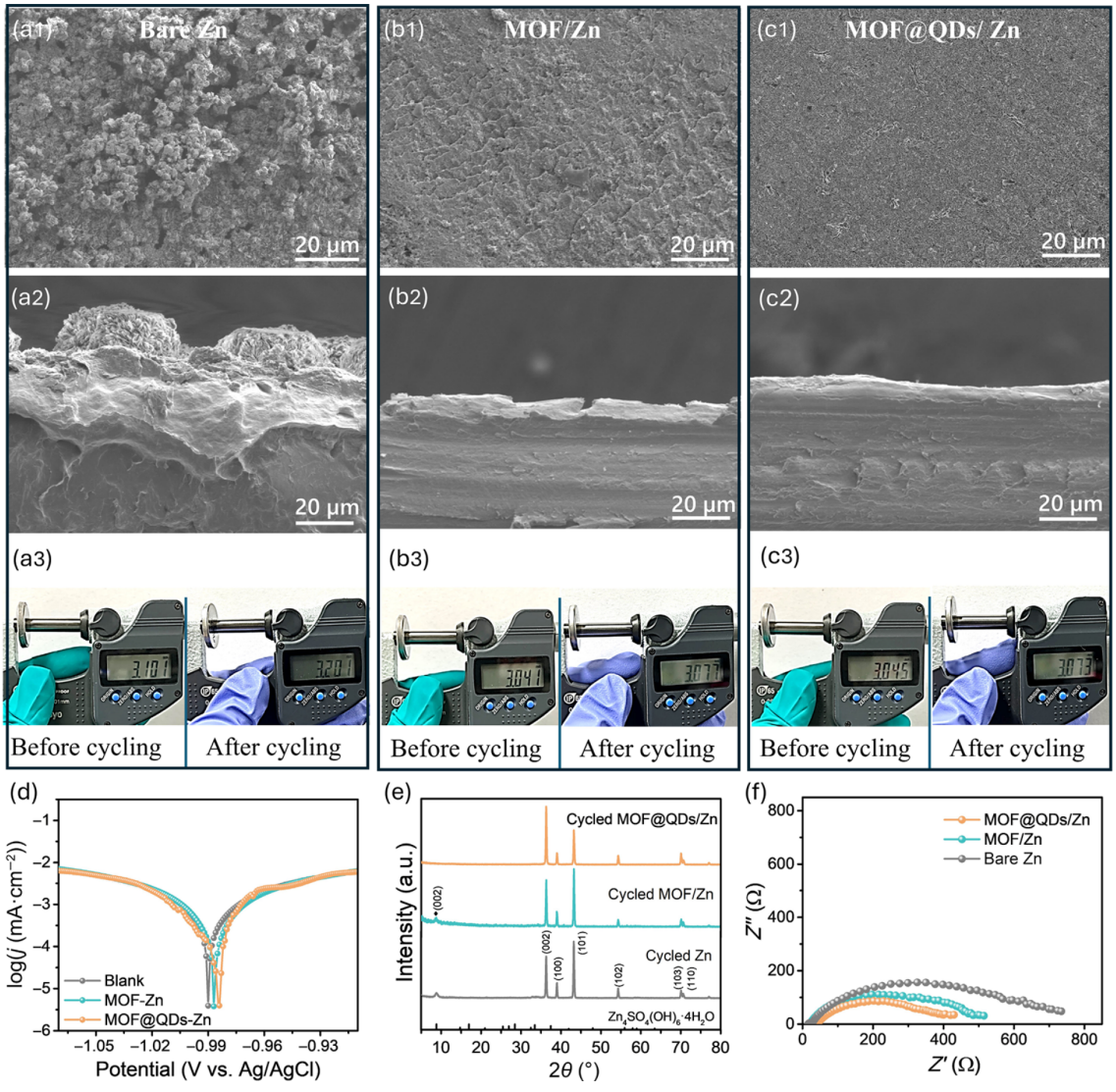

Figure 5 Top- and cross-sectional SEM images of Zn electrodes after 10 cycles in Zn//Zn cells with ((a1) and (a2)) bare Zn, ((b1) and (b2)) MOF/Zn, and ((c1) and (c2)) MOF@QDs/Zn. Volume expansion measurement of symmetrical cells for (a3) bare Zn, (b3) MOF/Zn, and (c3) MOF@QDs/Zn after 100 h of stripping/plating process. (d) Linear polarization curves of bare Zn, MOF/Zn, and MOF@QDs/Zn electrodes. (e) XRD patterns and (f) EIS comparison after 10 cycles in the symmetrical cells.

$Zn_4SO_4(OH)_6{\cdot}4H_2O$ (ZSH, JCPDS No. 44-0673) appears in the XRD patterns of MOF/Zn and bare Zn after cycling, implying that the ZSH by-product is formed due to an increased pH value resulting from the occurrence of the HER [41, 59]. In contrast, the MOF@QD microlayer effectively inhibits side reactions upon cycling, realizing high reversibility of the Zn plating/stripping reaction. Raman spectra of the bare Zn and MOF-modified Zn anodes exhibit peaks at 984, 1028, 1130, and 1177 cm^{-1} (Fig. S12 in the ESM), corresponding to the by-products of ZSH. In contrast, these peaks are not detected on the cycled MOF@QD/Zn, suggesting the suppression of by-products originating from the OH^-. To further verify the charge-transfer enhancement introduced by the QDs, the electronic conductivity (σ_e) of ZIF-8 and ZIF-8@QDs was measured using a potentiostatic polarization method (Fig. S13 in the ESM). At room temperature, the σ_e value of ZIF-8 was 1.84×10^{-8} $S{\cdot}cm^{-1}$, which is consistent with previously reported data [60]. In contrast, the σ_e of the ZIF-8@QDs composite increased to 4.24×10^{-7} $S{\cdot}cm^{-1}$, one order of magnitude higher than that of pristine ZIF-8, thereby demonstrating that $Ti_3C_2T_x$ QDs significantly facilitate charge transfer within the MOF@QDs/Zn anode. Meanwhile, the fast charge-transfer is also identified by the lower charge-transfer resistance (R_{ct}) of MOF@QD/Zn from the EIS results (Fig. 5(f)).

To evaluate the practical applicability of the modified Zn anode, Zn||MnO_2 full cells were assembled employing high-purity MnO_2 (Fig. S14 in the ESM) as the cathode material. In addition, 0.2 M $MnSO_4$ was added to 2 M $ZnSO_4$ electrolytes to prevent the dissolution of MnO_2 during the charge–discharge process [61]. The CV profiles of Zn full-cells with bare and modified Zn anodes delivered a similar shape at the scan rate of 0.1 $mV{\cdot}s^{-1}$ (Fig. 6(a)), which corresponds to the reversible redox reactions between MnO_2 and MnOOH [62]. Notably, the CV curve of MOF@QDs/Zn exhibits the highest current peaks and narrowest voltage gap between the redox peaks, suggesting decreased electrochemical polarization and corrosion passivation, thereby improving the Zn^{2+} ion transfer kinetics and reversibility of the electrochemical process [13]. Additionally, the galvanostatic profiles obtained for different Zn anodes at 0.2 $A{\cdot}g^{-1}$ are shown in Fig. 6(d). A higher discharge

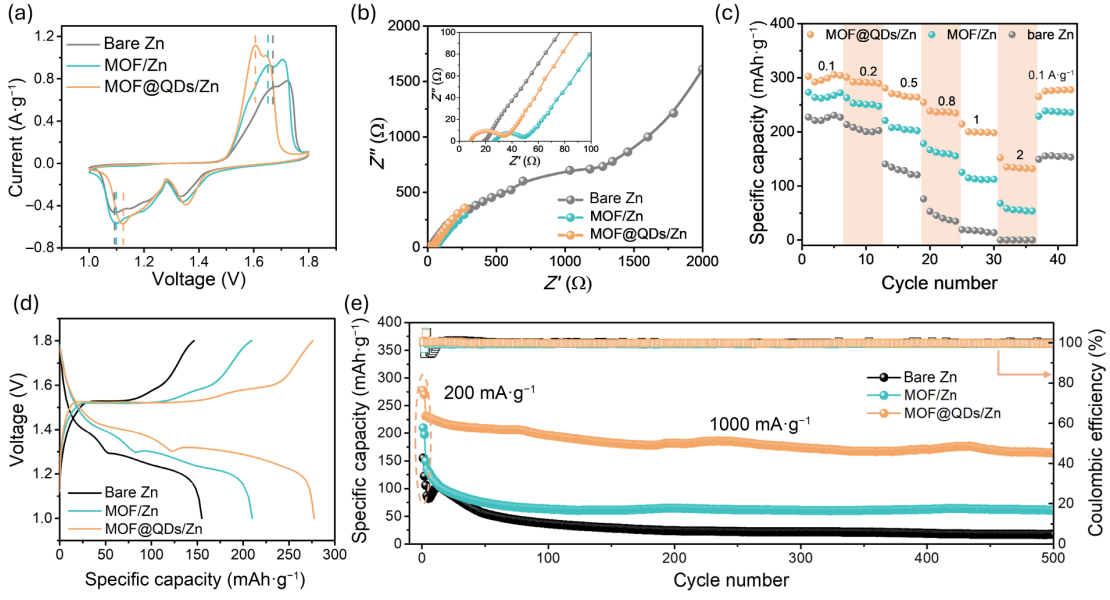

Figure 6 Electrochemical performance of Zn||MnO_2 full cells. (a) CV profiles at a scan rate of 0.1 mV·s^{-1}. (b) Nyquist plots and (c) rate capability of full cells with different anodes. (d) Galvanostatic charge–discharge profiles at 0.2 A·g^{-1}, and (e) cycling stability of full batteries at 1 A·g^{-1} with bare Zn, MOF/Zn, and MOF@QDs/Zn electrodes.

plateau and lower charge plateau are observed for MOF@QDs/Zn compared with those of the cells with MOF/Zn and pristine Zn anodes, further confirming the reduced voltage hysteresis, which agrees well with the CV measurement results. The fast reaction kinetics and low polarization of the cell with MOF@QDs/Zn may be ascribed to its low charge–discharge resistance, as shown by the EIS analysis in Fig. 6(b). Based on these contributions, a rate performance with excellent reversibility and high capacity was achieved for the battery with MOF@QDs/Zn (Fig. 6(c)). At a current density of 0.1 A·g^{-1}, the MOF@QDs/Zn electrode delivered a specific capacity of 302.3 mAh·g^{-1}, which is significantly higher than those of the bare Zn (227.2 mAh·g^{-1}) and MOF/Zn (273.2 mAh·g^{-1}) cells. Remarkably, the MOF@QDs/Zn anode maintained a considerable capacity of 135 mAh·g^{-1} even when the current density was increased to 2 A·g^{-1}. Upon returning the current density to 0.1 A·g^{-1}, the capacity recovered to an average value of 297.5 mAh·g^{-1}, indicating excellent reversibility of the Zn electrode after modification with the MOF@QDs microlayer. MOF/Zn delivered a lower average capacity (< 50 mAh·g^{-1}) at a high current density of 2 A·g^{-1}, due to the sluggish electron transport and fracture of the thick MOF layer on the anode. The charge–discharge profiles recorded at increased current densities from 0.1 to 2 A·g^{-1} are shown in Figs. S15(a)–S15(c) in the ESM. Due to severe dendrite formation and corrosion of the Zn anode, the cell with bare Zn exhibits the lowest rate capacity, along with rapid capacity fading during long-term cycling. As presented in Fig. 6(e), the capacities of the bare Zn and MOF/Zn full cells quickly decreased to 37 and 63 mAh·g^{-1}, respectively, within the first 100 cycles at 1 A·g^{-1}. In contrast, the MOF@QDs/Zn electrode delivered an impressive initial capacity of 277 mAh·g^{-1} at 1 A·g^{-1} and retained 166 mAh·g^{-1} after 500 cycles, corresponding to a capacity retention of 60%. Meanwhile, an ultrahigh CE of > 99.5% for the whole cycling process is observed. Therefore, the MOF@QD composite can be an efficient protective microlayer on the Zn anode that promotes both ion and electron transfer and regulates Zn deposition on the anode, thereby inhibiting dendrite growth and corrosion of the Zn metal to achieve enhanced performance.

4 Conclusions

In summary, we demonstrated the construction of dual ion–electron transport channels through *in-situ* growth of a $Ti_3C_2T_x$ quantum-dot-embedded ZIF-8 protective layer as a rational strategy for stabilizing Zn metal anodes. The ZIF-8 matrix with sub-nanopores enables uniform Zn^{2+} flux regulation while selectively screening out larger solvated clusters, effectively suppressing dendrite formation, hydrogen evolution, and surface corrosion. Simultaneously, the conductive $Ti_3C_2T_x$ QDs establish interconnected electron pathways within the insulating framework, accelerating interfacial charge transfer. Benefiting from these synergistic effects, the modified Zn anodes exhibit remarkably stable plating/stripping over 1200 cycles at 1 mA·cm^{-2} and 2000 cycles at 5 mA·cm^{-2}, with low overpotentials and dendrite-free deposition. Furthermore, Zn//MnO_2 full cells deliver high initial capacities (277 mAh·g^{-1} at 0.2 A·g^{-1}), excellent cycling retention (60% after 500 cycles at 1 A·g^{-1}), and ultra-high Coulombic efficiency (99.5%). These results highlight embedding conductive quantum-dots in MOF matrices as an effective approach to integrate ionic sieving and electronic conduction, thereby offering a universal design principle for advanced artificial interphases in Zn-based energy storage systems.

Electronic Supplementary Material: Supplementary material (TEM images, SEM images, Zeta potential measurement, Raman spectra, and more electrochemical tests) is available in the online version of this article at https://doi.org/10.26599/NR.2026.94908363.

Data availability

All data needed to support the conclusions in the paper are presented in the manuscript and the Electronic Supplementary Material. Additional data related to this paper may be requested from the corresponding author upon request.

Acknowledgements

This work was supported by the National Research Foundation of Korea (No. NRF-2021R1A2C1008272). This work was supported by the QingLan Project of Jiangsu Province.

Declaration of competing interest

All the contributing authors report no conflict of interests in this work.

Author contribution statement

M. L.: Data curation, writing manuscript, experimental design. T. C.: Data curation, project administration, validation. J. B.: Project administration, revising manuscript, supervision. All the authors have approved the final manuscript.

Use of AI statement

None.

References

[1] Chao, D. L.; Zhou, W. H.; Xie, F. X.; Ye, C.; Li, H.; Jaroniec, M.; Qiao, S. Z. Roadmap for advanced aqueous batteries: From design of materials to applications. *Sci. Adv.* **2020**, *6*, eaba4098.

[2] Yang, J. Z.; Yin, B. S.; Sun, Y.; Pan, H. G.; Sun, W. P.; Jia, B. H.; Zhang, S. W.; Ma, T. Y. Zinc anode for mild aqueous zinc-ion batteries: Challenges, strategies, and perspectives. *Nano-Micro Lett.* **2022**, *14*, 42.

[3] Zhang, W. J.; Sun, T. J.; Su, J. F.; Li, H. X.; Tao, Z. L. Ultra-low cost and high Coulombic efficiency aqueous zinc-ion battery. *Nano Res.* **2025**, *18*, 94907708.

[4] Liu, S. L.; Zhang, R. Z.; Mao, J. F.; Zhao, Y. L.; Cai, Q.; Guo, Z. P. From room temperature to harsh temperature applications: Fundamentals and perspectives on electrolytes in zinc metal batteries. *Sci. Adv.* **2022**, *8*, eabn5097.

[5] Li, C.; Jin, S.; Archer, L. A.; Nazar, L. F. Toward practical aqueous zinc-ion batteries for electrochemical energy storage. *Joule* **2022**, *6*, 1733–1738.

[6] Li, B.; Ruan, P. C.; Xu, X. Y.; He, Z. X.; Zhu, X. Y.; Pan, L.; Peng, Z. Y.; Liu, Y. Y.; Zhou, P.; Lu, B. G. et al. Covalent organic framework with 3D ordered channel and multi-functional groups endows Zn anode with superior stability. *Nano-Micro Lett.* **2024**, *16*, 76.

[7] Shang, Y.; Kundu, D. A path forward for the translational development of aqueous zinc-ion batteries. *Joule* **2023**, *7*, 244–250.

[8] Zhang, R. Y.; Xu, H.; Li, Z. M.; Dou, H.; Zhang, X. G. Regulation of ion transport behavior in layer-by-layer assembled polymer/MXene heterostructure anodes for metal-free aqueous zinc ion batteries. *Adv. Funct. Mater.* **2025**, *35*, 2424649.

[9] Wu, H. Y.; Yan, W.; Xing, Y. M.; Li, L.; Liu, J. Y.; Li, L.; Huang, P.; Lai, C.; Wang, C.; Chen, W. H. et al. Tailoring the interfacial electric field using silicon nanoparticles for stable zinc-ion batteries. *Adv. Funct. Mater.* **2024**, *34*, 2213882.

[10] Zhou, T. Y.; Mu, Y. L.; Chen, L.; Li, D. X.; Liu, W.; Yang, C. K.; Zhang, S. B.; Wang, Q.; Jiang, P.; Ge, G. L. et al. Toward stable zinc aqueous rechargeable batteries by anode morphology modulation via polyaspartic acid additive. *Energy Storage Mater.* **2022**, *45*, 777–785.

[11] Xue, P.; Guo, C.; Li, L.; Li, H. P.; Luo, D.; Tan, L. C.; Chen, Z. W. A MOF-derivative decorated hierarchical porous host enabling ultrahigh rates and superior long-term cycling of dendrite-free Zn metal anodes. *Adv. Mater.* **2022**, *34*, 2110047.

[12] Zhang, N. N.; Huang, S.; Yuan, Z. S.; Zhu, J. C.; Zhao, Z. F.; Niu, Z. Q. Direct self-assembly of MXene on Zn anodes for dendrite-free aqueous zinc-ion batteries. *Angew. Chem., Int. Ed.* **2021**, *60*, 2861–2865.

[13] Guo, C.; Huang, X.; Huang, J. L.; Tian, X.; Chen, Y. T.; Feng, W. H.; Zhou, J.; Li, Q.; Chen, Y. F.; Li, S. L. et al. Zigzag hopping site embedded covalent organic frameworks coating for Zn anode. *Angew. Chem., Int. Ed.* **2024**, *63*, e202403918.

[14] Yang, H. J.; Chang, Z.; Qiao, Y.; Deng, H.; Mu, X. W.; He, P.; Zhou, H. S. Constructing a super-saturated electrolyte front surface for stable rechargeable aqueous zinc batteries. *Angew. Chem., Int. Ed.* **2020**, *59*, 9377–9381.

[15] Huang, S. Y.; Fu, H.; Kwon, H. M.; Kim, M. S.; Zhang, J. D.; Lu, J.; Kim, J. S.; Jang, G.; Min, D. H.; Il Kim, W. et al. Stereoisomerism of multi-functional electrolyte additives for initially anodeless aqueous zinc metal batteries. *Nat. Commun.* **2025**, *16*, 6117.

[16] Yang, K.; Fu, H.; Duan, Y. X.; Ma, Z. H.; Wang, D.; Li, B. L.; Park, H. S.; Ho, D. Poloxamer pre-solvation sheath ion encapsulation strategy for zinc anode–electrolyte interfaces. *ACS Energy Lett.* **2024**, *9*, 209–217.

[17] Fu, H.; Huang, S. Y.; Wang, T.; Lu, J.; Xiong, P. X.; Yao, K.; Byun, J. S.; Li, W. W.; Kim, Y.; Park, H. S. Synergistic cationic shielding and anionic chemistry of potassium hydrogen phthalate for ultrastable Zn–I_2 full batteries. *Adv. Mater.* **2025**, *37*, 2411686.

[18] Huang, S. Y.; Zhang, P.; Lu, J.; Kim, J. S.; Min, D. H.; Byun, J. S.; Kim, M. J.; Fu, H.; Xiong, P. X.; Yoo, P. J. et al. Molecularly engineered multifunctional imide derivatives for practical Zn metal full cells. *Energy Environ. Sci.* **2024**, *17*, 7870–7881.

[19] Zhou, J. H.; Xie, M.; Wu, F.; Mei, Y.; Hao, Y. T.; Li, L.; Chen, R. J. Encapsulation of metallic Zn in a hybrid MXene/graphene aerogel as a stable Zn anode for foldable Zn-ion batteries. *Adv. Mater.* **2022**, *34*, 2106897.

[20] Wang, Z. R.; Zhang, Y. C.; Jiang, H. Y.; Wei, C. L.; An, Y. L.; Tan, L. W.; Xiong, S. L.; Feng, J. K. Free-standing $Na_2C_6O_6$/MXene composite paper for high-performance organic sodium-ion batteries. *Nano Res.* **2023**, *16*, 458–465.

[21] Chandra Sekhar, M.; Purusottam Reddy, B.; Kuchi, C.; Kamal Basha, C.; Al-Zahrani, F. A. M.; Mangiri, R. Enhanced solar-driven photocatalytic hydrogen production, dye degradation, and supercapacitor functionality using MoS_2–TiO_2 nanocomposite. *Ceram. Int.* **2024**, *50*, 38679–38687.

[22] Kuang, L. Y.; Xu, B. H.; Zhang, L.; Lin, Z. S.; Gu, X. X.; Ren, X. L.; Hou, Y. L. Zincophilic and hydrophobic bifunctional PFA-COOH-CNT artificial SEI film for highly stable Zn anode. *Nano Res.* **2025**, *18*, 94907156.

[23] Liu, M. Y.; Zhang, L. M.; Rostami, J.; Zhang, T.; Matthews, K.; Chen, S.; Fan, W. J.; Zhu, Y.; Chen, J. W.; Huang, M. H. et al. Tough MXene-cellulose nanofibril ionotronic dual-network hydrogel films for stable zinc anodes. *ACS Nano* **2025**, *19*, 13399–13413.

[24] Yu, H. M.; Chen, Y. J.; Wei, W. F.; Ji, X. B.; Chen, L. B. A functional organic zinc-chelate formation with nanoscaled granular structure enabling long-term and dendrite-free Zn anodes. *ACS Nano* **2022**, *16*, 9736–9747.

[25] Mangiri, R.; Ramachandran, T.; Kumar, Y. A.; Ghosh, A.; Al-Sehemi, A. G.; Yadav, A. K.; Mani, D. Surface engineering of M_5X_4 MXenes for next-gen energy solutions. *Mater. Today Chem.* **2025**, *48*, 102864.

[26] Li, M.; Song, S.; Li, Y.; Chen, T.; Bae, J. DNA-guided Li_2S nanostructure deposition for high-sulfur-loaded Li–S batteries. *ACS Appl. Nano Mater.* **2023**, *6*, 11037–11048.

[27] Sher, F.; Hayward, A.; El Guerraf, A.; Wang, B. H.; Ziani, I.; Hrnjić, H.; Boškailo, E.; Chupin, A.; Nemţanu, M. R. Advanced metal–organic frameworks for superior carbon capture, high-performance energy storage and environmental photocatalysis—A critical review. *J. Mater. Chem. A* **2024**, *12*, 27932–27973.

[28] Li, M.; Chen, T.; Song, S.; Li, Y.; Bae, J. HKUST-1@IL-Li solid-state electrolyte with 3D ionic channels and enhanced fast Li^+ transport for lithium metal batteries at high temperature. *Nanomaterials (Basel)* **2021**, *11*, 736.

[29] Chen, T.; Reddy, N. P.; Li, M. Enhancing solid-state Li-ion batteries with MOF-polymer composite electrolytes-effect mechanisms and interface engineering. *Gels* **2025**, *11*, 946.

[30] Li, M.; Song, S.; Li, Y.; Chu, M. M.; Chen, T.; Seung Lee, C.; Bae, J. Novel DNA-based polysulfide sieves incorporated with MOF providing excellent 3D Li^+ pathway for high-performance lithium–sulfur batteries. *Appl. Surf. Sci.* **2023**, *614*, 156163.
[31] Yuan, N.; Sun, W. D.; Yang, J. L.; Gong, X. R.; Liu, R. P. Multifunctional MOF-based separator materials for advanced lithium–sulfur batteries. *Adv. Mater. Interfaces* **2021**, *8*, 2001941.
[32] Chen, R. W.; Zhang, G. Y.; Zhou, H. J.; Li, J. R.; Li, J. T.; Chung, L. H.; Hu, X. H.; He, J. Robust zinc anode enabled by sulfonate-rich MOF-modified separator. *Small* **2024**, *20*, 2305687.
[33] Zhou, T.; Shen, J. D.; Wang, Z. S.; Liu, J.; Hu, R. Z.; Ouyang, L. Z.; Feng, Y. Z.; Liu, H.; Yu, Y.; Zhu, M. Regulating lithium nucleation and deposition via MOF-derived Co@C-modified carbon cloth for stable Li metal anode. *Adv. Funct. Mater.* **2020**, *30*, 1909159.
[34] Liu, L.; Xu, Q.; Zhu, Q. L. Electrically conductive metal–organic frameworks for electrocatalytic applications. *Adv. Energy Sustainability Res.* **2021**, *2*, 2100100.
[35] Zhang, Q.; Luan, J. Y.; Tang, Y. G.; Ji, X. B.; Wang, H. Y. Interfacial design of dendrite-free zinc anodes for aqueous zinc-ion batteries. *Angew. Chem., Int. Ed.* **2020**, *59*, 13180–13191.
[36] Wu, Z. L.; Zuo, Y. Z.; Zhang, Y. Z.; Li, X.; Zhang, J.; Wang, Y. L.; Shen, C. Y.; Cheng, X. M.; Liu, M. N.; Liu, H. T. et al. Modulating inner Helmholtz layer by electrocatalytically sieving $[Zn(H_2O)_6]^{2+}$ for 10,000-cycle zinc-ion hybrid capacitors under extremely harsh conditions. *Energy Storage Mater.* **2024**, *70*, 103463.
[37] Lu, X. J.; Chen, L.; Li, W. X.; Zhang, X. L.; Chi, W. L.; Peng, M.; Wang, C. X.; Liu, Y.; Zhang, X. W. Accelerating desolvation and constructing dual-storage channels for Zn^{2+} by ligand field engineering of polar organic molecules for high-performance zinc-ion batteries. *Adv. Funct. Mater.*, in press, DOI: 10.1002/adfm.202513457.
[38] Wang, Z. J.; Hu, S. L.; Wang, D.; Huang, J. J.; Qi, J. W.; Liu, H.; Li, X. F.; Han, C. P.; Cheng, H. M. A HER-inhibiting layer based on M–H bond regulation for achieving stable zinc anodes in aqueous zinc-ion batteries. *Adv. Funct. Mater.* **2025**, *35*, 2502186.
[39] Zhu, J. C.; Tie, Z.; Bi, S. S.; Niu, Z. Q. Towards more sustainable aqueous zinc-ion batteries. *Angew. Chem., Int. Ed.* **2024**, *63*, e202403712.
[40] Lee, Y. R.; Jang, M. S.; Cho, H. Y.; Kwon, H. J.; Kim, S.; Ahn, W. S. ZIF-8: A comparison of synthesis methods. *Chem. Eng. J.* **2015**, *271*, 276–280.
[41] Han, W. W.; Lee, H.; Liu, Y. Z.; Kim, Y.; Chu, H. Q.; Liu, G. C.; Yang, W. Toward highly reversible aqueous zinc-ion batteries: Nanoscale-regulated zinc nucleation via graphene quantum-dots functionalized with multiple functional groups. *Chem. Eng. J.* **2023**, *452*, 139090.
[42] Nguyen, D. N.; Gund, G. S.; Jung, M. G.; Roh, S. H.; Park, J.; Kim, J. K.; Park, H. S. Core–shell structured MXene@carbon nanodots as bifunctional catalysts for solar-assisted water splitting. *ACS Nano* **2020**, *14*, 17615–17625.
[43] Liu, C. L.; Bai, Y.; Wang, J.; Qiu, Z. M.; Pang, H. Controllable synthesis of ultrathin layered transition metal hydroxide/zeolitic imidazolate framework-67 hybrid nanosheets for high-performance supercapacitors. *J. Mater. Chem. A* **2021**, *9*, 11201–11209.
[44] Zhao, Z. M.; Zhao, J. W.; Hu, Z. L.; Li, J. D.; Li, J. J.; Zhang, Y. J.; Wang, C.; Cui, G. L. Long-life and deeply rechargeable aqueous Zn anodes enabled by a multifunctional brightener-inspired interphase. *Energy Environ. Sci.* **2019**, *12*, 1938–1949.
[45] Chen, S. M.; Ying, Y. R.; Ma, L. T.; Zhu, D. M.; Huang, H. T.; Song, L.; Zhi, C. Y. An asymmetric electrolyte to simultaneously meet contradictory requirements of anode and cathode. *Nat. Commun.* **2023**, *14*, 2925.
[46] Ju, J. G.; Zhang, Y.; Zhang, Y. X.; Zhang, Z. H.; Chen, S.; Zhao, C. F.; Kang, W. M. Robust zinc anode modification layer with hydrophobic-cation selectivity for stabilized aqueous zinc ion batteries. *Chem. Eng. J.* **2024**, *481*, 148479.
[47] Hong, L.; Wu, X. M.; Wang, L. Y.; Zhong, M.; Zhang, P. Y.; Jiang, L. S.; Huang, W.; Wang, Y. L.; Wang, K. X.; Chen, J. S. Highly reversible zinc anode enabled by a cation-exchange coating with Zn-ion selective channels. *ACS Nano* **2022**, *16*, 6906–6915.
[48] Zhao, W.; Perera, I. P.; Khanna, H. S.; Dang, Y. L.; Li, M. X.; Posada, L. F.; Tan, H. Y.; Suib, S. L. Modification of zinc anodes by *in-situ* ZnO coating for high-performance aqueous zinc-ion batteries. *ACS Appl. Energy Mater.* **2024**, *7*, 1172–1181.
[49] Mwemezi, M.; Prabakar, S. J. R.; Han, S. C.; Park, W. B.; Seo, J. Y.; Sohn, K. S.; Pyo, M. Zinc anodes modified by one-molecular-thick self-assembled monolayers for simultaneous suppression of side-reactions and dendrite-formation in aqueous zinc-ion batteries. *Small* **2022**, *18*, 2201284.
[50] Han, L. S.; Guo, Y. M.; Ning, F. H.; Liu, X. Y.; Yi, J.; Luo, Q.; Qu, B. H.; Yue, J. L.; Lu, Y. F.; Li, Q. Lotus effect inspired hydrophobic strategy for stable Zn metal anodes. *Adv. Mater.* **2024**, *36*, 2308086.
[51] Tian, C. Y.; Li, W. W.; Liu, X. W.; Zhang, D. T.; Wang, Y. Y.; Li, C. Y.; Wang, Y. Q.; Zhao, B.; Wang, M. F.; Li, M. P. et al. Hydrophobic organic–inorganic hybrid surface modification-induced uniform zinc deposition and prohibited side reactions toward a ultra-stable zinc anode. *ACS Sustainable Chem. Eng.* **2023**, *11*, 3576–3584.
[52] Chen, H. Q.; Wang, Y. Y.; Zhang, S. J.; He, Y. T.; Hou, L. R.; Yuan, C. Z. Two-pronged approach to achieving high-capacity and long stable-life aqueous Zn-ion batteries. *Chem. Eng. J.* **2024**, *479*, 147422.
[53] Khamsanga, S.; Uyama, H.; Nuanwat, W.; Pattananuwat, P. Polypyrrole/reduced graphene oxide composites coated zinc anode with dendrite suppression feature for boosting performances of zinc ion battery. *Sci. Rep.* **2022**, *12*, 8689.
[54] Liu, J. S.; Chen, S.; Shang, W. S.; Ma, J. Z.; Zhang, J. T. *In-situ* formation of 3D ZIF-8/MXene composite coating for high-performance zinc-iodine batteries. *Adv. Funct. Mater.* **2025**, *35*, 2422081.
[55] Sun, C.; Wu, C. P.; Gu, X. X.; Wang, C.; Wang, Q. H. Interface engineering via $Ti_3C_2T_x$ MXene electrolyte additive toward dendrite-free zinc deposition. *Nano-Micro Lett.* **2021**, *13*, 89.
[56] Li, D.; Long, J. Y.; Liu, X. Y.; Chen, X. L.; Li, Z. H.; Lei, G. T. Simple MOF composite coating-modified zinc metal anode for aqueous zinc-ion batteries. *Energy Fuels* **2025**, *39*, 8742–8752.
[57] Ou, Z. X.; Li, X.; Wang, Y.; He, D. X.; Gan, W.; Yuan, Q. H. Ionic sieve 2D-MOF modified anode for long durable aqueous zinc ion battery with high capacity. *Electrochim. Acta* **2025**, *523*, 145987.
[58] Bi, D.; Zhao, T. T.; Lai, Q. X.; Zhao, J. X.; Grigoriev, S. A.; Liang, Y. Y. *In-situ* preparation of MOF-74 for compact zincophilic surfaces enhancing the stability of aqueous zinc-ion battery anodes. *J. Alloys Compd.* **2024**, *1002*, 175448.
[59] Yang, X. Z.; Li, C.; Sun, Z. T.; Yang, S.; Shi, Z. X.; Huang, R.; Liu, B. Z.; Li, S.; Wu, Y. H.; Wang, M. L. et al. Interfacial manipulation via *in-situ* grown ZnSe cultivator toward highly reversible Zn metal anodes. *Adv. Mater.* **2021**, *33*, 2105951.
[60] Butler, K. T.; Worrall, S. D.; Molloy, C. D.; Hendon, C. H.; Attfield, M. P.; Dryfe, R. A. W.; Walsh, A. Electronic structure design for nanoporous, electrically conductive zeolitic imidazolate frameworks. *J. Mater. Chem. C* **2017**, *5*, 7726–7731.
[61] Zhang, X. L.; Chen, L.; Orenstein, R.; Lu, X. J.; Wang, C. X.; Yanilmaz, M.; Peng, M.; Dong, Y. C.; Liu, Y.; Zhang, X. W. Zincophilic and hydrophobic groups of surfactant-type electrolyte additive enabled stable anode/electrolyte interface toward long-lifespan aqueous zinc ion batteries. *Energy Storage Mater.* **2024**, *70*, 103500.
[62] Pan, H. L.; Shao, Y. Y.; Yan, P. F.; Cheng, Y. W.; Han, K. S.; Nie, Z. M.; Wang, C. M.; Yang, J. H.; Li, X. L.; Bhattacharya, P. et al. Reversible aqueous zinc/manganese oxide energy storage from conversion reactions. *Nat. Energy* **2016**, *1*, 16039.